Enantioselective Synthesis of Amino Acids by Photocatalytic Reduction of CO_2 on Chiral Mesostructured ZnS

Yongping Cui[1†], Jing Ai[2†], Yingying Duan[3†], Menghui Jia[5], Junhong Liu[1,4], Xi Liu[1,4], Tianwei Ouyang[1], Chaoyang Chu[6], Yuanbo Li[3], Yanhang Ma[6], Liwei Chen[1,4], Lu Han[3]*, Jinquan Chen[5]*, Shunai Che[1]*& Yuxi Fang[1]*

[1]School of Chemistry and Chemical Engineering, Frontiers Science Center for Transformative Molecules, State Key Laboratory of Metal Matrix Composites, Shanghai Key Laboratory for Molecular Engineering of Chiral Drugs, Shanghai Jiao Tong University, 800 Dongchuan Road, Shanghai, 200240, China. [2]Sinopec Shanghai Research Institute of Petrochemical Technology, 1658 Pudong Beilu, Shanghai, 201208, China. [3]School of Chemical Science and Engineering, Tongji University, 1239 Siping Road, Shanghai, 200092, China. [4]School of Chemical Science and Engineering, In-situ Centre for Physical Science, Shanghai Jiao Tong University, 800 Dongchuan Road, Shanghai, 200240, China. [5]State Key Laboratory of Precision Spectroscopy, East China Normal University, Shanghai, 200241, China. [6]Shanghai Key Laboratory of High-resolution Electron Microscopy & School of Physical Science and Technology, Shanghai Tech University, Shanghai, 201210, China.

† These authors contributed equally to this work. e-mail: sjtu15901600323@sjtu.edu.cn; chesa@sjtu.edu.cn; luhan@tongji.edu.cn; jqchen@lps.ecnu.edu.cn

Reduction and fixation of CO_2 in natural systems *via* solar energy generates diverse products, ranging from small molecules to biomolecules. To date, only a few multicarbon species have been obtained by artificial CO_2 photoreduction[1-5], especially abiotic photosynthesis of biomolecules with various functional groups, which has long been a fundamental yet challenging issue. Herein, we report the photocatalytic synthesis of amino acids from CO_2 and NH_3 on a chiral mesostructured ZnS (CMZ) nanosphere, which is constructed by arrays of chiral nanorods. Serine (Ser) is the main component of various amino acids, with an enantiomeric excess (*ee*) greater than 96% and a total yield of over 30 μmol g_{cat}^{-1}. The Ser formation pathway could be accessed through *OCCO intermediates due to C-C coupling, as demonstrated by experimental data. Chiral-induced spin polarization of CMZ has been speculated to facilitate the separation of photogenerated carriers and the production of stable triplet OCCO. Different activation energies of reduction reactions driven by the spin-polarized electrons in CMZ lead to the formation of enantiomeric amino acids. Our findings will inspire new perspectives in catalytic theory and the formation of chiral biomolecules in artificial synthesis and nature.

In CO_2 reduction, C-C coupling through CO dimerization is the important process to synthesize C_{2+} products[6-8]. OCCO formed by CO dimerization[9,10] was predicted to be converted into chemisorbed *$OCCO^-$ on the catalyst surface, leading to subsequent reactions[11]. However, the OCCO intermediate is converted from a metastable triplet into an unstable singlet that dissociates rapidly to two CO molecules, consequently terminating C-C coupling[12]. Spin-polarized materials have been known to exhibit high activity in photocatalytic oxygen evolution reactions owing to their excellent photocharge transfer properties and ability to promote the production of triplet O_2 in parallel aligned electrons[13-15]. In our previous works, it was found that various chiral mesostructured inorganic materials exhibit remarkable spin polarization through electron motions of transfer and transition[16-18] due to chiral induced spin selectivity **(**CISS) effect[19-22].

Herein, our approach is to endow chirality with ZnS to activate the unconventional C_{3+} production pathway of photocatalytic synthesis of amino acids from CO_2 and NH_3. ZnS was selected as a photocatalyst because it exhibits an ideal electronic structure for photocatalytic CO_2 reduction (Supplementary Fig. 1)[23]. Spin polarization of chiral mesostructured ZnS (CMZ) increase the photocharge transfer properties and promote metastable triplet OCCO by creating a parallel aligned electron environment. Spin-polarized electrons in CMZ make the synthesis of amino acids enantioselective due to the different activation energies of each inverse electron spin between each amino acid enantiomer.

Fabrication of CMZ

CMZs were synthesized by hydrothermal reaction in a homogeneous solution composed of cysteine, zinc salt, ethanolamine, and deionized water at 160 °C (see Methods section and Supplementary Fig. 2 for details). The amino acid cysteine (L- and D-Cys) was chosen as the sulfide source and symmetry-breaking agent. ZnS crystals with a chiral structure can be formed by a co-self-assembly effect, which results from the electrostatic interaction between Cys and Zn^{2+} ions through asymmetric attachment. Pure CMZ can be obtained by removing organics through washing precipitates. The absence of organic residue on CMZs was confirmed by high-performance liquid chromatography–mass spectrometry (HPLC–MS) and X-ray photoelectron spectroscopy (XPS) (Supplementary Fig. 3). The samples synthesized with L- and D-Cys were denoted as L- and D-CMZ, respectively. For comparison, achiral mesostructured ZnS (AMZ) was prepared using achiral thiourea as the sulfide source instead of chiral Cys.

Characterization of CMZs

The X-ray diffraction (XRD) patterns (Fig. 1a) of antipodal CMZ and AMZ indicate a structure identical to the wurtzite-2H phase of ZnS (JCPDS No. 36-1450) with a space group of *P*63*mc*[24]. The intensity of the (002) reflections of all samples is significantly higher than that of the bulk sample, suggesting that the ZnS nanorods were grown along the [001] reflection.

Scanning electron microscopy (SEM) images show that L-CMZ is composed of urchin-like nanospheres with a diameter distribution in the range of 500–700 nm (Fig. 1b and c). The nanospheres are constructed by tightly self-assembled radial arrays of hexagonal nanorods with a diameter of *ca.* 10 nm and a length in the range of 30-300 nm (Fig. 1d and Supplementary Fig. 4). High-resolution transmission electron microscopy (HRTEM) and high-angle annular dark-field scanning transmission electron microscopy (HADDF-STEM) images further confirm the urchin-like structures (Supplementary Fig. 4a-f). The nanorod showed the typical contrast of the hexagonal structure along the [001] hex direction, which agrees with the XRD observations, and a typical single nanorod with a lattice spacing of 3.1 Å corresponds to the (002) of the wurtzite-2H phase ZnS[24] (Supplementary Fig. 4h).

The helical structure of L-CMZ nanorods was characterized by HADDF-STEM observations (Fig. 1f). Notably, only the left part of the nanorod could align with the zone axis, while the right region gradually tilted away from the electron beam. Upon sequential left-handed tilting along the axial direction, the well-aligned region (indicated by the yellow box) gradually moved from the left to the right side. Fourier diffractograms (FDs) were taken at the local positions of the nanorod to judge the alignment of the corresponding regions[25]. A left-handed twisting lattice structure of helical ZnS nanorods was determined with an approximate 3° of rotation along the c-axis over a distance of 19 nm, suggesting a tilting angle of 0.16° nm^{-1}. HRTEM and STEM images were taken from individual CMZ nanorods along [100] and [1$\bar{1}$0] directions, in which the predominantly exposed facets are (010), (001) and (110) lattice planes (Supplementary Fig. 5). The morphology and structure of D-CMZ and AMZ are similar to that of L-CMZ (Supplementary Figs. 6 and 7).

XPS shows that the binding energy peak positions of Zn^{2+} and S^{2-} are almost identical in CMZs and AMZ, indicating a similar surface state of both chiral and achiral structures (Supplementary Fig. 8). Brunauer-Emmett-Teller (BET) specific surface areas of antipodal CMZs (119.0 and 122.2 m^2g^{-1}) are smaller than that of AMZ (172.4 m^2g^{-1}) (Supplementary Fig. 9 and Table 1).

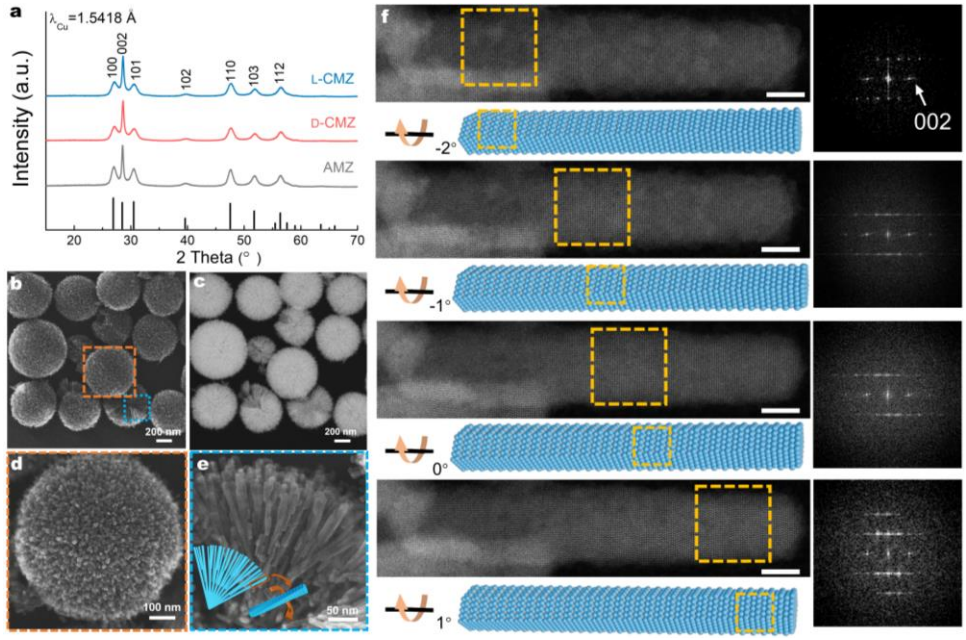

Fig. 1 | Structures and morphologies of CMZ. a, Powder XRD patterns of the antipodal CMZ and AMZ. **b, c,** Low-magnification SEM (**b**) and corresponding STEM (**c**) images of L-CMZ. **d, e,** Representative SEM images of L-CMZ at various magnifications. **f**, HADDF-STEM images of an L-CMZ nanorod. The nanorod is helical, and the zone axis can only align with the incident electron beam upon consecutively tilting the crystal along its [001] hex axis by -2°, -1°, 0° and 1°. The scale bar is 3 nm. The synthetic molar composition was Zn^{2+}:Cys:EA:H_2O = 1:2:58.3:1600.

Photocarrier properties of CMZ

Fig. 2a presents UV–Vis diffuse reflectance spectra (UV–Vis DRS) of antipodal CMZs and AMZ. Three samples show similar absorption at a wavelength of *ca.*350 nm, attributed to the electron transition from Zn 4*d* (valence band, VB) to S 3*p* (conductor band, CB). The optical band gaps calculated from DRS show the values of *ca.* 3.35, 3.39 and 3.44 eV for L-CMZ, D-CMZ and AMZ (inset of Fig. 2a), respectively, in slightly increasing order.

The photoluminescence (PL) and femtosecond time-resolved transient absorption spectra (TAS) were measured to provide electron-hole recombination properties. As illustrated in Fig. 2b, the PL peak intensity of antipodal CMZ at 361 nm[28] is lower than that of AMZ, even if the light harvesting is enlarged in the opposite profile, as observed from UV–Vis DRS (Fig. 2a). This result indicates that the photocarrier separation capability of CMZ is stronger than that of AMZ. The lifetime of the photocarrier was calculated from TAS (Supplementary Fig. 10) to be 962.3, 911.4 and 888.2 ps for L-CMZ, D-CMZ and AMZ, respectively. No other peaks were observed in PL, indicating that there are no other dislocations, Zn^{2+} vacancies, or S^{2-} vacancies in CMZ than in AMZ [30].

The photoinduced electron transfer of CMZ was investigated by the time dependence of the photocurrent (Supplementary Fig. 11a). The antipodal CMZ exhibited a higher current density of *ca.* 40 μA cm^{-2} than AMZ (*ca.* 5 μA cm^{-2}) for *ca.* 8 times, which demonstrates the delayed recombination kinetics of electron-hole pairs and highly efficient charge transfer. The Nyquist plot electrochemical impedance spectra (EIS) show that compared to AMZ, the antipodal CMZ has a smaller electrochemical resistance, indicating that a more favourable charge transfer is present in CMZ (Supplementary Fig. 11b).

Spin polarization of CMZ

The spin polarization of CMZ has been investigated by magnetic tip conducting atomic force microscopy (mc-AFM) *via* tunneling conductance depending on the polarized spin of the tip[26] (Supplementary Fig. 12). Fig. 2c shows that the current in the L-CMZ was significantly and slightly changed with increasing bias voltage when the tip was magnetized in the UP and DOWN directions, respectively, indicating spin-UP polarization in L-CMZ[26]. The opposite behavior indicates the spin DOWN polarization deduced in D-CMZ. A chirality induced effective magnetic field, $\mathbf{B}_{chiral}$, results in spin polarization of the other depending on the handedness of the CMZ due to the CISS effect (*vide post* for detail in Fig. 2f). As expected, the conduction is not spin-specific in AMZ (Supplementary Fig. 13), illustrating no spin polarization in achiral structure. A weak current at a negative bias potential results from the rectification effect of ZnS[27].

The chirality and spin polarization of the CMZs were further characterized using a circular dichroism (CD) spectrometer. Fig. 2d illustrates the mirror-image CD spectra of the antipodal CMZs at *ca.* 330 nm[28]. This observation further validates their handedness observed in electron microscopy images. The CD absorbance peak position of CMZ differs from that of Cys molecules (Supplementary Fig. 14). The observed CD signals of CMZ can be considered as the superposition of two circular dichroic sources (Supplementary Fig. 15a): (i) Natural CD (NCD) signals arising from the spatial redistribution of the net charge, combining a magnetic dipole transition moment and a magnetic dipole transition moment ($\boldsymbol{\mu}\cdot\boldsymbol{m}$)[29]. In L-CMZ with a left-handed chiral center, right-handed circular polarization is dominantly absorbed, resulting in a negative NCD signal, and *vice versa* in D-CMZ. (ii) CD signals arising from spin polarization induced by the $\mathbf{B}_{chiral}$ due to the movement of electrons in a helical potential. The UP spins polarized in L-CMZ preferred to absorb right-handed circular polarization, resulting in a negative CD signal. In other words, more UP spins in L-CMZ will be excited to transition from VB to CB. The presence of $\mathbf{B}_{chiral}$ was confirmed by external magnetic field-dependent asymmetric magnetic circular dichroism (MCD) spectra (Supplementary Fig. 15 and 16)[20]. As expected, AMZ shows silent spectra due to the absence of chiral structures and positive and negative cancellations.

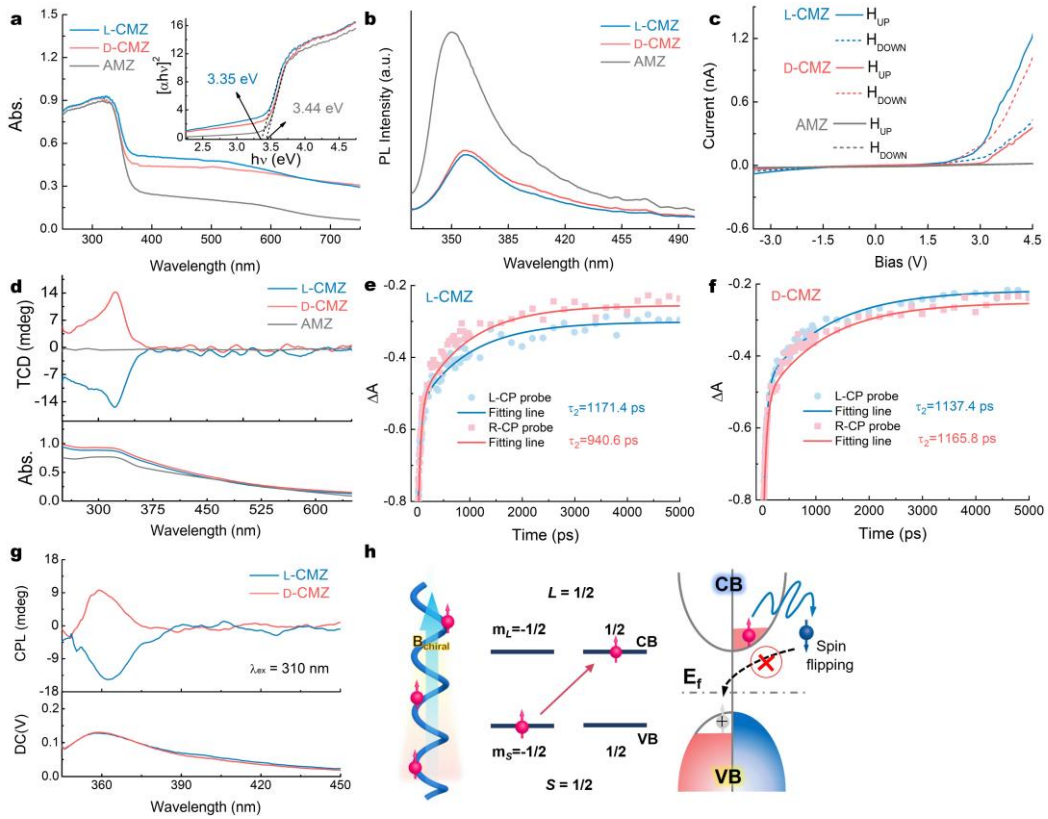

Fig. 2 | Spin polarization and photoexcited charge separation properties of the samples. a, UV–Vis DRS. The inset shows the Tauc plots obtained from DRS by plotting $[\alpha h\nu]^2$ versus $h\nu$. α and ν are the absorbance coefficient and light frequency, respectively. **b,** PL spectra at an excitation wavelength of 315 nm. **c,** I-V curves obtained from mc-AFM measurements on the antipodal CMZ under Xe lamp irradiation. **d,** DRUV–Vis and transmitted CD spectra. **e, f,** CPTAS of antipodal CMZs, measured with linear polarized pump and different circularly polarized probe beams at a probe wavelength of 360 nm. **g,** CPL spectra of antipodal CMZs at an excitation wavelength of 310 nm. **h**, Schematic drawing of spin polarization suppressing photocarrier recombination in L-CMZ.

The dynamics of photoexcited charge carriers and spin states in CB of CMZs were investigated using circularly polarized transient-absorption spectroscopy (CPTAS, Supplementary Fig. 17 for detailed mechanisms). Spin-DOWN and spin-UP electrons in CB were distinguished based on their lifetimes (τ_2) measured using L-CP and R-CP probes, respectively. A longer τ_2 indicates a more dominant spin. As shown Fig. 2e and f (Supplementary Table 3), in L-CMZ, it is evident that the τ_2 probed with L-CP is longer than that with R-CP probe, suggesting that spin-DOWN electrons are dominant in the CB of L-CMZ, and *vice versa* in D-CMZ. As expected, in AMZ, τ_2 of spin-DOWN and spin-UP electrons in the CB are almost the same (Supplementary Fig. 18). This finding implies that in L-CMZ, the predominantly excited spin-UP electrons observed in CD and MCD spectra are inverted to the spin-DOWN state.

The spins returned from CB to the VB were investigated through circularly polarized luminescence (CPL) spectra (Supplementary Fig. 19). As shown in Fig. 2g, the antipodal CMZs exhibit opposite polarization emissions with λ_{max}=350 nm owing to the violet emission region for a signature of electron-hole recombination in ZnS nanocrystals. As the inverse process of excitation, the CPL spectrum of L-CMZ shows a negative peak, indicating that more UP spins are return to the VB and preferentially emit R-CP light. From the results of CPTAS and CPL, it can be inferred that UP spins tend to return to VB and DOWN spins tend to remain in the excited state in the CB.

The photoexcited electrons should satisfy the conservation of spin angular momentum. Form the above characterizations, it can be predicted that the electrons in the CB undergo spin flipping and are inversed from their original spin direction during the charge-transfer process due to the strong asymmetric spin-orbital coupling (SOC) in the CMZ [13,15,31]. In L-CMZ, the spin-UP polarized photoexcited electrons is inversed to spin-DOWN, and *vice versa* in D-CMZ. These electrons cannot return to the VB due to spin filter channels and remain in the CB as free electrons[31-33] (Fig. 2h) and are utilized for photocatalysis.

Formation of enantiomeric excess amino acids by photocatalytic reduction of CO_2 on CMZs

Previously, photocatalytic synthesis of amino acids utilizing CO_2 are photocarboxylation of organic amines with CO_2[34-36]. CO_2 was activated to CO_2^- and organic amines were activated to α-amino radicals for accomplishing carboxylation in previous works. In this work, the strategy is forming α-keto acids by photocatalytic reduction of CO_2 as an exclusive carbon source. Subsequently, synthesize amino acids by amination of α-keto acids by NH_3.

To synthesize amino acids *via* photocatalytic reduction of CO_2, $NH_3{\cdot}H_2O$ was selected as the nitrogen source (see Methods). To ensure that the chiral structural effect of CMZ and to exclude the effect of chiral molecules on the catalytic activity, L-Cys-adsorbed AMZ (L-Cys-AMZ) with loading 5.27 mol% of L-Cys was prepared for comparison (Supplementary Fig. 20).

Fig. 3a and b show the yields of products generated from antipodal CMZ, AMZ and Cys-AMZ (Supplementary Fig.21 and Table 4). Total amino acid yields of 32.1 μmol g_{cat}^{-1} on average were achieved by using antipodal CMZ as the photocatalyst (Fig. 3a). On antipodal CMZ, the yields of serine (Ser), glycine (Gly), alanine (Ala) and other amino acids are 12.9, 12.8, 3.2 and 3.1 μmol g_{cat}^{-1} on average, respectively; these values are *ca.* 31 times higher than those obtained with AMZ. Notably, in a control experiment using L-Cys-AMZ as a catalyst, the CO_2 reduction product yields are as low as that of AMZ, indicating that the chiral structure plays a key role in catalysis rather than L-Cys.

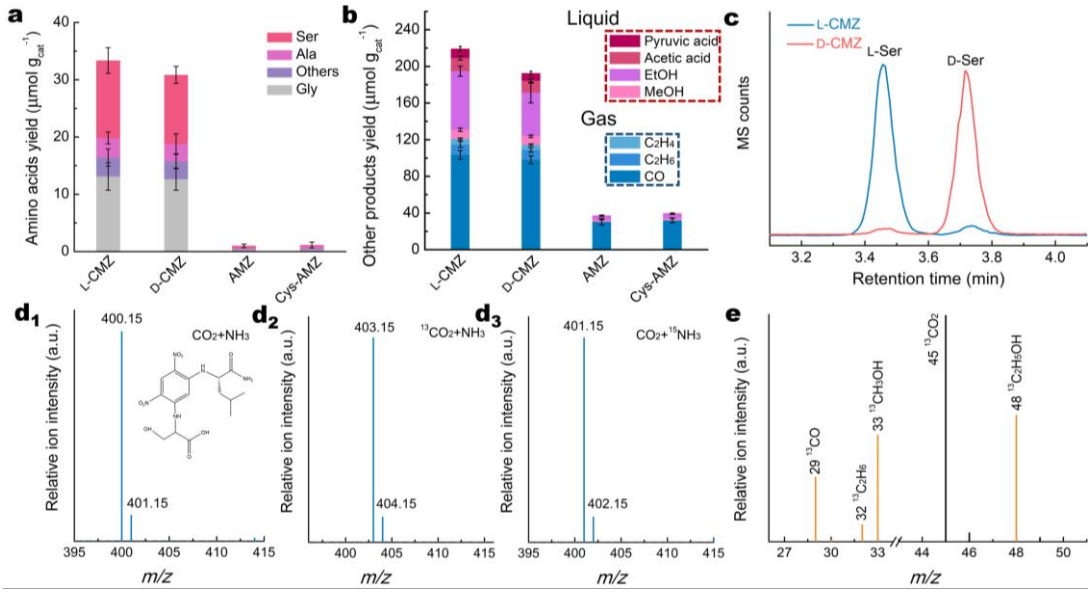

Fig. 3 | Photocatalytic performances of the catalysts. a, Yield of amino acids. **b,** Yield of other products. Error bars represent the standard deviation of measurements based on the five independent samples. **c,** HPLC-MS analysis of antipodal Ser produced on L- and D-CMZ as photocatalysts. **d,** HPLC-MS spectrum of the Ser after CO_2 and $NH_3{\cdot}H_2O$ (**d$_1$**), $^{13}CO_2$ and $NH_3{\cdot}H_2O$ (**d$_2$**), CO_2 and $^{15}NH_3{\cdot}H_2O$ (**d$_3$**) photoreduction for the L-CMZ. Inset of d: the molecular structure of l-FDLA derivatized Ser. e, GC-MS spectrum of the products after 13CO2 photoreduction for the l-CMZ. Typical CO2 photoreduction experiment was carried out with 15 mg catalyst dispersed in 60 mL 1M $NH_3{\cdot}H_2O$ aqueous solution, under 1.5 MPa CO_2 atmosphere in a stainless-steel reactor with a xenon lamp irradiation for 12 h.

Moreover, the amino acids were confirmed to be synthesized from CO_2 as a carbon source and NH_3 as a nitrogen source by using different contrast experiments (Supplementary Fig. 22). The results of a series of control experiments revealed that the formation of amino acids depends on the photocatalytic activity of CMZ (Supplementary Figs. 23-26). The other product yields of antipodal CMZ were also higher than AMZ (Fig. 3b and Supplementary Fig. 27). The average yields of CO and C_{2+} products of L-CMZ are *ca.* 101.6 and 136.3 μmol g_{cat}^{-1}, 3.5 and 13.6 times higher than that of AMZ, respectively. The C_{2+} selectivity of CMZ is 57.3%, which is an *ca.* 2.6 times as that of AMZ, indicating promoted C-C coupling in chiral materials.

The *ee* value of Ser produced over CMZ was determined by HPLC–MS after derivatization by N-(5-fluoro-2,4-dinitrophenyl)-L-leucinamide (L-FDLA)[37] (Supplementary Fig. 28). As shown in Fig. 3c, L- and D-Ser derivatives were observed at retention times of 3.47 and 3.73 min, respectively. In the L- and D-CMZ photocatalytic systems, antipodal Ser with *ee* values of 96.0± 0.5% was achieved.

To further elucidate the sources of carbon and nitrogen in the products, isotope-labeling experiments using $^{13}CO_2$ and $^{15}NH_3$ were conducted. Fig. 3d and e present the HPLC-MS and gas chromatography-mass spectrogram (GC-MS) spectra of Ser and other catalytic products. The HPLC-MS analysis revealed that 97.18% and 95.74% of Ser products were determined to be ^{13}C and ^{15}N-labeled, respectively, which were identified by peaks with mass-to-charge ratios of m/z=403.15 for ^{13}C and m/z=401.15 for ^{15}N-labeled Ser. The presence of unlabeled Ser was speculated to originate from the environment and unlabeled impurities in $^{13}CO_2$ and $^{15}NH_3$. Simultaneously, a mixed product consisting of ^{13}CO (*m*/*z*=29) and $^{13}C_2H_6$ (*m*/*z*=32), $^{13}CH_3OH$ (*m*/*z*=33) and $^{13}C_2H_5OH$ (*m*/*z*=48) was yielded on L-CMZ. Additionally, other amino acids were obtained in isotope-labeling experiments (Supplementary Fig. 29). These results confirm that the generated amino acids indeed originated from the photoreduction of CO_2 and NH_3.

Pathway and mechanism for the formation of amino acids from CO_2 reduction

To detect the reaction intermediates in the CO_2 photoreduction process, in situ diffuse reflection infrared Fourier transform spectroscopy (DRIFTS) measurements were performed. As shown in Fig. 4a (see also Supplementary Fig. 30a and b), the intensity of the main peaks increases at 1,040 and 2,971 cm^{-1}, corresponding to the stretching vibration of C-N and the amino group (-NH_2) on amino acids, respectively (Supplementary Fig. 30c). These observations suggest that amino acids continually form from the reaction of CO_2 and NH_3. The peaks at 910, 1,229 and 1,398 cm^{-1} could be assigned to 3-hydroxypyruvic acid[38] which would be intermediate of Ser formation. The peaks at 1,922 cm^{-1} could be attributed to *CO species[39]. The peaks at 1,180, 1,561, and 1,872 cm^{-1} are estimated to attribute to *HOCCO and *$OCCO^-$[40,41], which would be the intermediate for the formation of C_{2+} products. The IR peak of the *HOCCO and *$OCCO^-$ on the CMZ surfaces were calculated by density functional perturbation theory (DFPT) (Supplementary Fig. 31), which match their peaks in DRIFTS.

A reasonable mechanism for the activation of CO_2 photoreduction to amino acids may involve spin polarization-based promoted production and stabilization of *OCCO intermediates as well as photocarrier properties of CMZ. Based on the photocatalytic CO_2 reduction mechanism for C_1-C_2 products[2-5, 42-45], mechanism of C-C coupling *via* OCCO[11, 45, 46] and electrosynthesis of amino acids from CO_2 reduction[47], we proposed a possible pathway for amino acids formation from CO_2 and NH_3 (Fig. 4c and Supplementary Fig. 32).

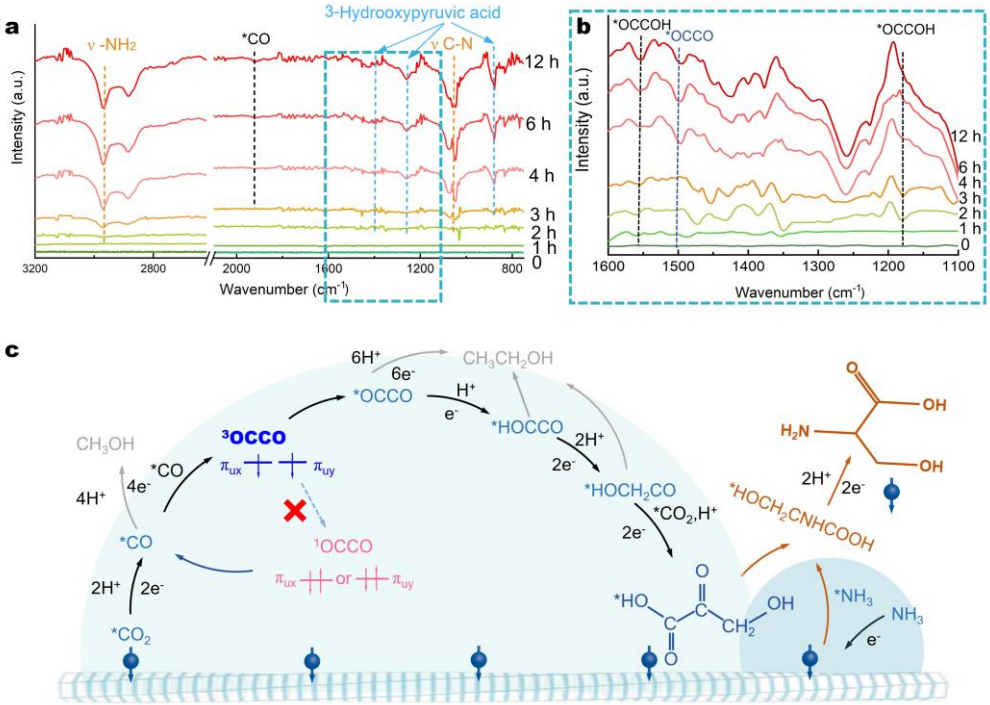

Fig. 4 | Investigation on the mechanism of photocatalytic CO_2 to chiral amino acids. a,b, In-situ DRIFTS of real-time photocatalytic reaction system on L-CMZ. **c,** Sketch showing the formation of amino acids on the CMZ catalyst with mediation by CO_2 and NH_3.

Adsorbed $*CO_2$ reacts into *CO, which subsequently dimerizes to OCCO[11]. OCCO is a triplet with unpaired electrons that occupy two degenerate Π orbitals in a neutral state[11]. The triplet state of OCCO is therorized to cross to the $^1\Delta_g$ singlet, which dissociates rapidly to two CO[12] (Supplementary Fig. 33). Triplet OCCO could be converted to stable reduced state, $*OCCO^-$[11, 46], which is the most important intermediate in the pathway. In the same manner as triplet O_2[13-15, 31], the triplet OCCO is speculated to be generated and more stable in parallel aligned electron spin than in antiparallel aligned electron spin. Spin polarization of CMZ makes electron spin aligned in a parallel fashion on its surfaces, which correlates with the formation and the stabilization of the OCCO. Thus, triplet OCCO can be rapidly formed on CMZ by dimerization of *CO and is adsorbed on CMZ to become *OCCO, which is reduced to $*OCCO^-$. Then, *HOCCO is formed by hydrogenation of $*OCCO^-$, which is hydrogenated to form $*HOCH_2CO$ successively. Similar to the acetyl-CoA pathway[48], the formation of 3-hydroxypyruvic acid is accomplished by the carboxylation of $*HOCH_2CO$ by CO_2. Then, Ser is synthesized *via* amination of 3-hydroxypyruvic acid with $*NH_3$.

Although Ser is the main product of amino acids, comparable amounts of Ala and Gly were produced. The synthesis pathway of Ala would be similar to Ser pathway, in which the $*HOCH_2CO$ is additionally deoxygenated to $*CH_3CO$. Then, the $*CH_3CO$ reacts with CO_2 to form pyruvic acid. Ala is synthesized by amination of pyruvic acid with $*NH_3$. Gly synthesis pathway would be started from the glyoxylic acid formed by hydrolysis of partial *OCCO that cannot be successfully converted into $*OCCO^-$ in the Ser pathway. Finally, the Gly is synthesized by amination of glyoxylic acid with $*NH_3$.

The high *ee* value of amino acids produced over CMZ can be speculated to be induced by enantioselective reactions due to spin polarization. It has been predicted that spin-polarized electrons ejected from magnetized magnetite can selectively interact with one-handedness as the interaction with the opposite-handedness is energetically penalized with the value of twice spin-orbit Hamiltonian, $2H_{SO}$[49,50]. The difference between the activation energies for L- and D- molecules causes a difference between the reaction rates for two isomers, which is the reason for the enantioselectivity of the reduction reaction. In the situation of amino acids formation by amination of α-keto acid, there could be a difference in reaction rate for last step hydrogenation between L- and D- enantiomers (Supplementary Fig. 34). Therefore, the spin-polarized electrons ejected from CMZ are supposed to break the chiral symmetry in the reduction reaction as they alter the reaction kinetics for enantiomers. The direction of the electron-spin polarization from CMZ defines the handedness of the amino acids.

Conclusions

To the best of our knowledge, the photocatalytic reduction of CO_2 into enantiomeric amino acids at room temperature is the first example of complex C_{3+} products with C-N and C=O bonds. The construction of the chiral structure in semiconductors provides an effective way to induce spin polarization and thus provides a new perspective for improving carrier dynamics and surface reactions in the photocatalytic reduction of CO_2. The spin polarization in the chiral structure was discovered to generate and stabilize the *OCCO intermediates to trigger the C-C coupling between C_2 species and C_1 species in the C_{3+} pathway and enantioselectivity in amino acid formation. This new method efficiently stabilizes *OCCO by parallel aligned electron spin, which is induced by spin polarization of the CISS effect of chiral materials. Importantly, the chiral amino acid was synthesized by using CO_2 and NH_3, inspiring new horizons into the reaction involving multiplet intermediates, asymmetric catalysis and carbon fixation for human consumption.

References

1. Halmann, M. Photoelectrochemical reduction of aqueous carbon dioxide on p-type gallium phosphide in liquid junction solar cells. *Nature* **275**, 115-116 (1978). DOI: 10.1038/275115a0
2. Rao, H., Schmidt, L., Bonin, J. & Robert, M. Visible-light-driven methane formation from CO_2 with a molecular iron catalyst. *Nature* **548**, 74-77 (2017). DOI: 10.1038/nature23016
3. Zhou, B. et al. Light-driven synthesis of C_2H_6 from CO_2 and H_2O on a bimetallic AuIr composite supported on InGaN nanowires. *Nat. Catal.* (2023). DOI: 10.1038/s41929-023-01023-1
4. Gao, W. et al. Vacancy-defect modulated pathway of photoreduction of CO_2 on single atomically thin $AgInP_2S_6$ sheets into olefiant gas. *Nat. Commun.* **12**, 4747

(2021). DOI: 10.1038/s41467-021-25068-7
5. Li, X. et al. Cocatalysts for selective photoreduction of CO_2 into solar fuels. *Chem. Rev.* **119**, 3962-4179 (2019). DOI: 10.1021/acs.chemrev.8b00400
6. Zhang, J. et al. Accelerating electrochemical CO_2 reduction to multi-carbon products via asymmetric intermediate binding at confined nanointerfaces. *Nat. Commun.* **14**, 1298 (2023). DOI: 10.1038/s41467-023-36926-x
7. Nitopi, S. et al. Progress and Perspectives of Electrochemical CO_2 Reduction on Copper in Aqueous Electrolyte. *Chem. Rev.* **119**, 7610-7672 (2019). DOI: 10.1021/acs.chemrev.8b00705
8. Wang, R. et al. Selective generation of electroreduction C_1–C_2 products through self-regulation of catalytically active Cu sites on the same coordination cluster catalyst. *CCS Chem.* **5**, 2237-2250 (2023). DOI: 10.31635/ccschem.022.202202316
9. Dixon, A. R., Xue, T. & Sanov, A. Spectroscopy of ethylenedione. *Angew. Chem. Int. Ed.* **54**, 8764-8767 (2015). DOI: 10.1002/anie.201503423
10. Katharine, G. et al. Spectroscopy of ethylenedione and ethynediolide: A reinvestigation. *Angew. Chem. Int. Ed.* **57**, 5394-5397 (2018). DOI: 10.1002/anie.201801848
11. Hedstrom, S. et al. Spin uncoupling in chemisorbed OCCO and CO_2: Two high-energy intermediates in catalytic CO_2 reduction *J. Phys. Chem. C* **122**, 12251-12258 (2018). DOI: 10.1021/acs.jpcc.8b02165
12. Mato, J., Poole, D. & Gordon, M. Stability and dissociation of ethylenedione (OCCO). *J. Phys. Chem. A* **124**, 8209-8222 (2020). DOI: 10.1021/acs.jpca.0c06107
13. Mtangi, W. et al. Control of electrons' spin eliminates hydrogen peroxide formation during water splitting. *J. Am. Chem. Soc.* **139**, 2794-2798 (2017). DOI: 10.1021/jacs.6b12971
14. Vadakkayil, A. et al. Chiral electrocatalysts eclipse water-splitting metrics through spin control. *Nat. Commun.* **14**, 1067 (2023). DOI: 10.1038/s41467-023-36703-w
15. Ai, M. et al. Spin selection in atomic-level chiral metal oxide for photocatalysis. *Nat. Commun.* **14**, 4562 (2023). DOI: 10.1038/s41467-023-40367-x
16. Liu, Z. et al. Photomagnetic-chiral anisotropy of chiral nanostructured gold films. *Chem* **8**, 186-196 (2022). DOI: 10.1016/j. Chempr.2020.10.003
17. Bai, T. et al. Chiral mesostructured NiO films with spin polarisation. *Angew. Chem. Int. Ed.* **60**, 9421-9426 (2021). DOI: 10.1002/anie.202101069
18. Bai, T. et al. Resistance-chiral anisotropy of chiral mesostructured half-metallic Fe_3O_4 films. *Angew. Chem. Int. Ed.* **60**, 20036-20041 (2021). DOI: 10.1002/anie.202108142
19. Metzger, T. S. et al. Optical activity and spin polarization: The surface effect. *J. Am. Chem. Soc.* **145**, 3972-3977 (2023). DOI: 10.1021/jacs.2c10456
20. Yang, S. H. Naaman, R. Paltiel & Parkin, S. S. Chiral spintronics. *Nat. Rev. Phys.* **3**, 328-343 (2021). DOI: 10.1038/s42254-021-00302-9
21. Ray, K., Ananthavel, S. P., Waldeck, D. H. & Naaman, R. Asymmetric scattering of polarized electrons by organized organic films of chiral molecules. *Science* **283**, 814-816 (1999). DOI: 10.1126/science.283.5403.814
22. Eckvahl, H. et al. Direct observation of chirality-induced spin selectivity in electron donor-acceptor molecules. *Science* **382**, 197-201 (2023). DOI: 10.1126/science.adj5328
23. Cheng, S. et al. Emerging strategies for CO_2 photoreduction to CH_4: From experimental to data-driven design. *Adv. Energy Mater.* **12**, 2200389 (2022). DOI: 10.1002/aenm.202200389
24. Xiong, et al. Tunable synthesis of various wurtzite ZnS architectural structures and their photocatalytic properties. *Adv. Funct. Mater.* **17**, 2728–2738 (2007). DOI: 10.1002/adfm.200600891
25. Duan, T. et al. Spontaneous chiral self-assembly of CdSe@CdS nanorods. *Chem* **7**, 1-13 (2021). DOI: 10.1016/j.chempr.2021.06.009
26. Kiran, V. et al. Helicenes—A new class of organic spin filter. *Adv. Mater.* **28**, 1957-1962 (2016). DOI: 10.1002/adma.201504725
27. Dalui, A. et al. Insight into the mechanism revealing the peroxidase mimetic catalytic activity of quaternary CuZnFeS nanocrystals: colorimetric biosensing of hydrogen peroxide and glucose. *Nanoscale* **7**, 9062-9074 (2015). DOI: 10.1039/C5NR01728A
28. Won, Y. H., et al. Highly efficient and stable InP/ZnSe/ZnS quantum dot light-emitting diodes. *Nature* **575**, 634–638 (2019). https://doi.org/10.1038/s41586-019-1771-5
29. Berova, N. Nakanishi, K. & Woody, R. W. *Circular Dichroism: Principles and Applications*, (Wiley-VCH, 2000).
30. Sookhakian, M. et al. Synthesis, structural, and optical properties of type-II ZnO-ZnS core-shell nanostructure. *J. Lumin.* **145** 244-252 (2014). DOI: 10.1016/j.jlumin.2013.07.032
31. Gao, W. et al. Electron spin polarization-enhanced photoinduced charge separation in ferromagnetic $ZnFe_2O_4$. *ACS Energy Lett.* **6**, 2129–2137 (2021). DOI: 10.1021/acsenergylett.1c00682
32. Lin, C. et al. Spin-polarized photocatalytic CO_2 reduction of Mn-doped perovskite nanoplates. *J. Am. Chem. Soc.* ***144*** (34), 15718-15726 (**2022**). DOI: 10.1021/jacs.2c06060
33. Lin, X. Han, Y. Zhu, J & Wu, K. Room-temperature coherent optical manipulation of hole spins in solution-grown perovskite quantum dots. *Nat. Nanotech.* **18**, 124-130 (2023). DOI: 10.1038/s41565-022-01279-x
34. Saini, S. et al. Visible light induced α-amino acid synthesis from carbon dioxide using nanostructured ZnO/CuO heterojunction photocatalyst. *Materialia* **12**, 100770 (2020). DOI: https://doi.org/10.1016/j.mtla.2020.100777
35. Mita, T., Chen, J., S, Masumi. and Sato, Y. One-Pot Synthesis of α-Amino Acids from CO_2 Using a Bismetal Reagent with Si-B Bond. *Org. Lett.* **14**, 6202-6205 (2012). DOI: https://doi.org/10.1021/ol302952r
36. Seo, H., Katcher, M. H. and Jamison, T. F. Photoredox activation of carbon dioxide for amino acid synthesis in continuous flow. *Nat. Chem.* **9**, 453-456 (2017). DOI: https://doi.org/10.1038/nchem.2690
37. Kobayashi, M. et al. Simplification of FDLA pre-column derivatization pro LC/MS/MS toward separation and detection of D, L-amino acids. *Chromatographia* **82**, 705–70810 (2019). DOI: 1007/s10337-018-3676-0
38. Gomes, J. F. et al. Influence of silver on the glycerol electro-oxidation over AuAg/C catalysts in alkaline medium: A cyclic voltammetry and in situ FTIR spectroscopy study. *Electrochim. Acta*, **144**, 361-368 (2014). DOI: 10.1016/j.electacta.2014.08.035
39. Gervillié-Mouravieff, C. et al. Unlocking cell chemistry evolution with operando fibre optic infrared spectroscopy in commercial Na (Li)-ion batteries. *Nat. Energy* **7**, 1157–1169 (2022). DOI: 10.1038/s41560-022-01141-3
40. Kim, Y. et al. Time-resolved observation of C–C coupling intermediates on Cu electrodes for selective electrochemical CO_2 reduction. *Energy Environ. Sci.* **13**, 4301 (2020). DOI: 10.1039/d0ee01690j
41. Zhang, Z. Y. et al. Cu-Zn-based alloy/oxide interfaces for enhanced electroreduction of CO_2 to C_{2+} products. *J. Energy Chem.* **83**, 90–97 (2023). DOI:10.1016/j.jechem.2023.04.034
42. Fang, S. et al. photocatalytic CO_2 reduction. *Nat. Rev. Method. Prime.* **3**, 61 (2023). DOI: 10.1038/s43586-023-00243-w
43. Chang, X. Wang, T. & Gong, J. CO_2 photo-reduction: insights into CO_2 activation and reaction on surfaces of photocatalysts. *Energy Environ. sci.* **9**, 2177-2196 (2016). DOI: 10.1039/C6EE00383D
44. Wang, Y. et al. Direct and indirect Z-scheme heterostructure-coupled photosystem enabling cooperation of CO_2 reduction and H_2O oxidation. *Nat. Commun.* **11**, 3043 (2020). DOI: 10.1038/s41467-020-16742-3
45. Jiang, M. et al. Magnetic-field-regulated TiO_2 {100} facets: A strategy for C-C coupling in CO_2 photocatalytic conversion. *Chem* **6**, 2335-2346 (2020). DOI: https://doi.org/10.1016/j.chempr.2020.06.033
46. Liu, P., Yang, Y & Wang, Q. Mechanism insights into direct conversion of syngas into C_2 oxygenates via key intermediate C_2O_2 over Ni-Supported graphene. *Carbon* **175**, 322-333 (2021). DOI: 10.1016/j.carbon.2021.01.008
47. Fang, Y. et al. Synthesis of amino acids by electrocatalytic reduction of CO_2 on chiral Cu surfaces. *Chem* **9**, 460-471 (2022). DOI: 10.1016/j.chempr.2022.10.017
48. Varma, S. J. et al. Native iron reduces CO_2 to intermediates and products of the acetyl-CoA pathway. *Nat. Ecol. Evol.* **2**(6), 1019 (2018). DOI: 10.1038/s41559-018-0542-2
49. Ozturka, S. F. & Sasselov, D. D. On the origins of life's homochirality: Inducing enantiomeric excess with spin-polarized electrons. *P. Natl. Acad. Sci. USA.* **119**(28), e2204765119 (2022). DOI: 10.1073/pnas.2204765119
50. Bhowmick, D. K. et al. Spin-induced asymmetry reaction-The formation of asymmetric carbon by electropolymerization. *Sci. Adv.* **8**, 2727-2734 (2021). DOI: 10.1126/sciadv.abq2727

Supplementary Information is available in the online version of the paper.

Acknowledgments

This work was supported by the National Key R&D Program of China (Grant No. 2021YFA1200301, S. C.), the National Natural Science Foundation of China (Grant No. 21931008, S. C.; 21975184, Y. D.) and Shanghai Pilot Program for Basic Research-Shanghai Jiao Tong University (21TQ1400219).

Author Contributions

Y. F. conceived the idea and led the project. Y. C. synthesized the materials, performed and analyzed the photochemical measurements, IR, SEM, XRD, CD, PL, DRS, XPS, MCD, AFM and carried out the catalysis; L. H., J. A., J. L., X. L., L. C., C. C. and Y. M., worked on the structural characterization through S/TEM and HRTEM; J. C., M. J. and Y. D. contributed to the measurement and analysis of lifetime and spin selectivity of materials; T. O. carried out the DFT calculation; Y. F., S. C. and Y. C. contributed to the analysis of mechanism and the preparation of the manuscript.

Competing interests

The authors declare no competing interests

Data availability

The data that support the findings of this study are available from the corresponding authors upon request. Source data are provided in this paper.

Additional information

Correspondence and requests for materials should be addressed to Yuxi Fang or Shunai Che.

METHODS:

Synthesis of CMZ and AMZ

All samples were synthesized by a facile hydrothermal method[24]. In a typical synthesis, Zn acetate (0.22 g, 1 mmol) and L-Cys (0.24 g, 2 mmol) were dissolved in deionized water (26.5 mL). Then, 3.5 mL ethylenediamine was added to the above solution and continually stirred for 15 min. The obtained solution was then transferred to a 50 mL Teflon-lined stainless-steel autoclave and heated to 160 °C for 15 h. After cooling to room temperature, the samples were collected by centrifugation, washed with ultrapure water several times, and dried in a vacuum oven at 50 °C. The synthesis of AMZ is similar to that of CMZ, in which thiourea (0.25 g, 2 mmol) was used as a sulfide source instead of L-Cys.

Morphology and structural characterizations of catalysts

The crystal structure of CMZ and AMZ was examined by powder XRD, which was collected on a Rigaku MiniFlex 600 X-ray diffractometer equipped with Cu Kα (λ=1.5418 Å) radiation working at an acceleration voltage of 40 kV and a current of 80 mA. The scanning rate was set to 0.05° $2\theta\ s^{-1}$ (θ, angle).

Aberration-corrected scanning transmission electron microscopy (S/TEM) was performed using a probe-corrected Hitachi HF5000 S/TEM operating at 200 kV. The instrument was equipped with bright field (BF), HAADF and secondary electron (SE) detectors for high spatial resolution STEM imaging experiments.

Low-magnification SEM images were obtained using a JEOL JSM-7800 with an accelerating voltage of 5.0 kV.

TEM and HRTEM images were obtained using a JEOL model JEM-2100F operated with a field-emission gun at 200 kV.

XPS

XPS was performed on an ESXCALAB Xi+ spectrometer (Thermo Fisher Corp.) with a 12 kV Al-Kα X-ray source with a step size of 0.1 eV. All the spectra were calibrated to the C 1s peak at 284.6 eV.

mc-AFM

mc-AFM Current-voltage (I-V) measurements were performed using Multimode AFM with Nanoscope V controller (Bruker-Dimensionicon). I-V spectroscopy measurements were recorded by performing a voltage bias of −6 to +6 V at the tip in a contact mode. For each spectroscopy measurement, the tip was placed in a new position. A magnetic Pt-coated Crtip (Multi75E-G, Budget Sensors) with nominal spring constant 3 N m^{-1} was used to acquire I-V curves. The tips are magnetized using a permanent magnet.

BET surface area

The nitrogen adsorption/desorption isotherms were measured at 77 K with a Quantachrome QDI-SI. The surface area was calculated by the Brunauer-Emmett-Teller (BET) method, and the pore size was obtained from the maxima of the pore size distribution curve calculated by the Barrett-Joyner-Halenda (BJH) method using the desorption branch of the isotherm.

CD spectra

CD spectra were obtained on a JASCO J-1500 spectropolarimeter fitted with a TCD apparatus, and data were collected with a scanning rate of 20 nm min^{-1} ranging from 190 to 800 nm at 293 K.

CD spectra under different magnetic fields were obtained on a JASCO J-1500 spectropolarimeter in TCD mode, which is equipped with an electromagnetic field range from 0.001 T to 1.500 T. The data were collected with a scanning rate of 20 nm min^{-1} ranging from 190 to 800 nm at 293 K under an antiparallel magnetic field.

CPL spectra

CPL spectra were obtained from a JASCO CPL-300 spectropolarimeter under the condition of scanning rate of 20 nm·min^{-1} ranging from 340 to 550 nm with step of 0.1 nm at the temperature of 293 K.

PL spectra

The PL spectra were collected on samples in air using a PTI QM/TM/IM with an exciting light wavelength of λ = 315 nm.

TAS and CPTAS

Femtosecond TAS experiments were carried out with a commercial spectrometer (Helios fire-EOS, Ultrafast Systems). The fundamental pulse was generated from a Ti: sapphire regenerative amplifier (Astrella, Coherent Inc., 800 nm, 100 fs, 7 mJ/pulse). A fraction of the fundamental beam was used to produce pump beams via an optical parametric amplifier (OPerA Solo, Coherent Inc.). A white light continuum (WLC) probe beam was generated by focusing the fundamental beam into a CaF_2 crystal, and the time window limit was 8 ns. The polarization between pump and probe pulses was set to be 54.7° during TA measurements. In CPTAS, L-CP and R-CP probe pulses were generated by using a quarter wave plate. 20 mg sample was dispersed in 1 mL of water and ultrasonically dispersed for 3 h.

Optical property analysis

The UV–Vis DRS was collected using a Lamda 950 UV–vis spectrophotometer with a scanning rate of 50 nm min^{-1} ranging from 250 to 750 nm.

The various bandgap energies (E_g) of CMZ and AMZ were attributed to the different mesostructures, which were calculated according to the reported formula:

$$[\alpha h\nu]^n = A(h\nu - E_g) \quad (1)$$

where n=2, representing ZnS, is a direct bandgap semiconductor. α and ν are the absorbance coefficient and light frequency, respectively.

Photoelectrochemical measurements

Transient photocurrent and EIS were measured in a conventional three-electrode process on an electrochemical workstation (CHI760E). Typically, a suspension was obtained by dispersing 5 mg samples into a 1 mL solution containing water and ethanol (v/v=1/4). The FTO conducting glass (1.1×10×20 mm) coating 0.1 mL of the suspension was the working electrode. Ag/AgCl and Platinum wire electrode were the reference electrode, and counter electrode, respectively. 0.5 M KCl aqueous solution served as the electrolyte.

CO_2 photochemical reduction

The photocatalytic CO_2 reduction was carried out in a closed system using a stainless reaction cell (150 mL) at 25 ℃. First, the catalyst (15 mg) was dispersed in a solution containing water (56 mL) and ammonium hydroxide (4 mL), and then the cell was degassed for 30 min before it was filled with ultra-pure CO_2 (>99.999%) to a pressure of 1.5 MPa. A 300 W Xe lamp (Beijing Ceaulight, CEL-HXF300-T3) sticks close to the window of the reactor as a light source, and the average light intensity irradiated on the photoreactor was *ca.* 100 mW cm^{-2}. Last, the gas was collected in an aluminum bag and then injected into the gas chromatograph instrument GC9720Plus (equipped with a TCD and an FID detector, Fuli) for quantitative analysis of the products for 12 h, where CH_4, CO, H_2, C_2H_4, C_2H_6 and CO_2 were detected. Liquid products were detected by 1H NMR spectroscopy (Bruker Advance-III 500).

According to our previous work[43], the photocatalytic production solution was centrifugated and evaporated at 70 °C overnight. The purified product was dissolved in 1 mL H_2O. The analysis of amino acids was carried out by using an L-8900 amino acid analyzer (Hitachi, Japan). An ion-exchange chromatographic column (L-8900, Hitachi, Japan) was adopted, where the amino acids were eluted by a lithium buffer system of an amino acid analyzer. After reacting with 500 μL of ninhydrin solution (979 mL of propylene glycol monomethyl ether, 39 g of ninhydrin, and 81 mg of sodium hydroxide), the resultant derivatives were measured by UV detection at two wavelengths of 440 and 570 nm simultaneously. Due to a low response at 570 nm, the derivative of proline was detected at 440 nm. Quantification of amino acids was performed using mixed amino acid standard solutions of Type B and Type A N-2 (Wako) using the same method mentioned above[43].

In our work, catalytic performance was described by production yield calculated via equations (2, 3 and 4).

The production yield of amino acid (Y_{aa}, μmol g_{cat}^{-1}),

$$Y_{aa} = n_{aa}/m_{cat} \quad (2)$$

Cumulative production (n_{aa}) was obtained by the report of the amino acid analyzer. m_{cat} is the mass of the catalyst.

Gas production yield (Y_g, μmol g_{cat}^{-1}),

$$Y_g = n_g/m_{cat} \quad (3)$$

Where n_g represents the production of a molecule in gas, obtained from $n_g = pV_g/RT$. p and V_g are the total pressure and partial volume of a molecule in gas phase. V_g was estimated by the GC report.

Liquid production yield (Y_l, μmol g_{cat}^{-1}),

$$Y_l = n_l/m_{cat} \quad (4)$$

Where n_l represents the production of a molecule in liquid phase, which was estimated from the report of 1H NMR using DMSO (0.01408 μmol dissolved in 600 μL measured liquid) as an internal standard substance.

Enantiomeric excessed amino acids analysis

The photocatalytic production solution was centrifugated and evaporated at 70°C overnight. The purified product was dissolved in 1 mL H_2O and then derivatized by L-FDLA before separation by HPLC-MS. To derivatize amino acid compounds, 50 μL of the obtained solution was mixed with 20 μL of 1 M sodium bicarbonate and 20 μL of 1% L-FDLA in acetone[34]. The mixture was incubated at 37 °C for 30 min. After returning to room temperature, 20 μL of 1 M HCl and 200 μL of methanol were added to the

sample, and the impurity was centrifuged (12000 rpm, 10 min). The sample was kept in the dark condition.

HPLC-MS analysis was performed by using an Acquity UPLC & XEVO G2-XS QTOF (Waters, United States) equipped with a UPLC column (Acquity UPLC HSS T3 1.8 μm, 2.1*100 mm). The detection of samples was conducted in positive ESI mode, and the function type was TOF-MS with a mass range of 200-600. Then, a 0.1 μL sample was injected and eluted using mobile phase A (0.1% mass concentration of formic acid aqueous solution) and mobile phase B (acetonitrile) at a flow rate of 0.35 mL/min. The programmed mobile phase gradient was as follows: 0.00–1.00 min, 25% B; 1.00–4.30 min 35% B; 4.30–6.50 min 100% B; 6.50–40 min 25% B. The column was equilibrated before sample injection, and the temperature of the column oven was set at 45 ℃.

To generate a standard curve of L- and D-Ser, the standard compounds were diluted in water at concentrations adjusted to be relevant to tissue contents. After derivatization, 10 μL of the standard solution was separated and detected using the HPLC-MS system.

The enantiomeric excess (*ee*) was calculated based on the integrated peak areas of L- and D-Ser as indicated in equation 5.

$$ee = (\text{L-Ser} - \text{D-Ser})/(\text{L-Ser} + \text{D-Ser}) \quad (5)$$

where L-Ser and D-Ser represent the obtained peak areas of L-FDLA-DERIVATIZED L-Ser and L-FDLA-derivatized D-Ser, respectively. The standard error of the mean of the % *ee* was calculated employing equation 6.

$$\text{s.e.m.} = S/n \quad (6)$$

where S is the standard deviation and n is the number of experiments.

In-situ DRIFTS measurements

DRIFTS measurements were conducted in situ. In brief, a Harrick Scientific HVCDRP reaction chamber coupled with a Praying Mantis DRIFTS accessory was employed. The base of the reaction cell was surrounded by a coil for cooling water circulation. The sample cup was set in the centre of the cell, which had three windows on its dome. Two domes (KBr type) were used for the transmission of infrared radiation and the left dome (quartz type) was used for light introduction from a 300 W Xe lamp.

Density functional theory (DFT) calculation

The DFT calculations of *OCCO and *OCCOH on the CMZ surfaces were done using the Vienna ab initio simulation package (VASP)[51-53]. performing a variational solution of the Kohn-Sham equations in a plane-wave basis with energy cutoff of 500 eV. All atomic positions in the complex were fully relaxed without symmetry restrictions using a conjugate-gradient algorithm, the convergence criteria for the energy and force of the atoms in the structural optimization are 1×10-7 eV and -1×10-7 eV/Å, respectively. Electron exchange correlation interactions were treated using the generalized gradient approximation as parameterized by Perdew, Burke and Ernzerhof[54]. The electron-ion interactions were described using the projector-augmented-wave (PAW) method[55]. The harmonic vibrational frequencies of *OCCO and *OCCOH on ZnS were calculated using density functional perturbation theory (DFPT), determining the Hessian matrix of the second derivatives of the energy with respect to the atomic positions and the vibrational frequencies[56-58], and obtain the matrix of Born effective charges (BEC) (the first derivative to the polarization with respect to the ionic coordinates). Within the dipole approximation the infrared intensity of an eigenmode was expressed in terms of the BEC and the eigenvectors as where the sum is over all atoms in the system[59].

51. Kresse, G. & Hafner, J. Ab initio molecular dynamics for liquid metals. *Phys. Rev. B* **47**, 558-561 (1993). DOI: 10.1103/PhysRevB.47.558
52. Kresse, G. & Hafner, J. Ab initio molecular-dynamics simulation of the liquid-metalamorphous- semiconductor transition in germanium. *Phys. Rev. B* **49**, 14251-14269 (1994). DOI: 10.1103/PhysRevB.49.14251
53. Kresse, G. & Furthmuller, J. Efficient iterative schemes for ab initio total-energy calculations using a plane-wave basis set. *Phys. Rev. B* **54**,11169-11186 (1996). DOI: 10.1103/physrevb.54.11169
54. Perdew, J.P., Burke, K. & Ernzerhof, M. Generalized gradient approximation made simple. *Phys. Rev. Lett.* **77**, 3865-3868 (1996). DOI: 10.1103/PhysRevLett.77.3865
55. Kresse, G. & Joubert, D. From ultrasoft pseudopotentials to the projector augmented-wave method. *Phys. Rev. B* **59**, 1758-1775 (1999). DOI: 10.1103/PhysRevB.59.1758
56. Baroni, S., de Gironcoli, S., Dal Corso, A. & Giannozzi, P. Phonons and related crystal properties from density-functional perturbation theory. *Rev. Mod. Phys.* **73**, 515-562 (2001). DOI: 10.1103/RevModPhys.73.515
57. Wu, X., Vanderbilt, D. & Hamann, D.R. Systematic treatment of displacements, strains, and electric fields in density-functional perturbation theory. *Phys. Rev. B* **72**, 035105 (2005). DOI: 10.1103/PhysRevB.72.035105
58. Gajdos, M. et al. Linear optical properties in the projector-augmented wave methodology. *Phys. Rev. B* **73**, 045112 (2006). DOI: 10.1103/PhysRevB.73.045112
59. Karhanek, D., Bucko, T. & Hafner, J. A density functional study of the adsorption of methane-thiol on the (111) surfaces of the Ni-group metals: I. Molecular and dissociative adsorption. *J. Phys. Condens. Matter* **22**, 265005 (2010). DOI: 10.1088/0953-8984/22/26/265006